RSC Advances

ROYAL SOCIETY OF CHEMISTRY

www.rsc.org/advances

Cite this: DOI: 10.1039/c0xx00000x

www.rsc.org/xxxxxx

ARTICLE TYPE

Enhanced photodegradation activity of methyl orange over Z-scheme type MoO_3/g-C_3N_4 composite under visible light irradiation

Yiming He*[a,e], Lihong Zhang[a], Xiaoxing Wang[a], Ying Wu[b], Hongjun Lin [c], Leihong Zhao[b], Weizheng Weng[d], Huilin Wan[d] and Maohong Fan*[e,f]

Received (in XXX, XXX) Xth XXXXXXXXX 20XX, Accepted Xth XXXXXXXXX 20XX
DOI: 10.1039/b000000x

Novel Z-scheme type MoO_3/g-C_3N_4 composites photocatalysts were prepared with a simple mixing-calcination method, and evaluated for their photodegradation activities of methyl orange (MO). The optimized MoO_3/g-C_3N_4 photocatalyst shows a good activity with a kinetic constant of 0.0177 min^{-1}, 10.4 times higher than that of g-C_3N_4. Controlling various factors (MoO_3/g-C_3N_4 amount, initial MO concentration, and pH value of MO solution) can lead to the enhancement of the phtocatalytic activity of the composite. Only MoO_3 and g-C_3N_4 are detected with X-ray diffraction (XRD) and Fourier transform infrared spectroscopy (FT-IR) spectra. N_2 adsorption and UV-vis diffuse reflectance spectroscopy (DRS) results suggest that the addition of MoO_3 slightly affects the specific surface area and the photoabsorption performance. The transmission electron microscopy (TEM) image of MoO_3/g-C_3N_4 indicates a close contact between MoO_3 and g-C_3N_4, which is beneficial to interparticle electron transfer. The high photocatalytic activity of MoO_3/g-C_3N_4 is mainly attributed to the synergetic effect of MoO_3 and g-C_3N_4 in electron-hole pair separation via the charge migration between the two semiconductors. The charge transfer follows direct Z-scheme mechanism, which is proven by the reactive species trapping experiment and the •OH-trapping photoluminescence spectra.

1. Introduction

Organic pollutants are present in the water environment usually as a result of industrial effluents. With the development of industry, the volume of wastewater containing nonbiodegradable pollutants have increased rapidly. Dealing with the pollutants demands the development of new, effective, clean, and safe decontamination technologies. Photocatalysis represents a promising alternative technology for degradation of organic pollutants in water, and hence attracts much attention [1]. Titanium oxide (TiO_2) has been used to degrade many organic pollutants in water and air [2-6]. It is considered as a promising photocatalyst since it is stable, insoluble, non-toxic, resistant to corrosion and relatively inexpensive. However, TiO_2 photocatalyst is effective only under irradiation of UV light due to its wide band gap. Many strategies, such as metal or nonmetal element doping [7-9], dye sensitization [10] and semiconductor coupling [11], have been applied to overcome the shortcoming. Cost-effective photocatalysts with high efficiencies under visible light are desired.

Currently, many scientists pay attention on the non-TiO_2 based photocatalyst and developed a lot of novel photocatalysts, such as Bi_2WO_6 [12], g-C_3N_4 [13], Ag_3PO_4 [14], AgBr [15], etc. Among them, g-C_3N_4 attracted a great deal of interests due to its good photoactivity, moderate band gap, and low cost. In addition, it is considered as a "sustainable" material since pure g-C_3N_4 is a metal-free semiconductor and can be synthesized by the simple calcination of urea and melamine at 500-600 °C [16-17]. Three approaches have been applied to promote its photocatalytic activity in degrading organics more efficiently: increasing the surface area [18-19], doping with metal or nonmetal elements [20-21], coupling with another semiconductor [22-23]. The last method was considered as the most feasible one, which has been applied to develop Pt/CdS/PdS composite with the highest quantum efficiency achieved so far [24]. Since Wang et al. first reported the photocatalytic activity of g-C_3N_4 [13], a varity of g-C_3N_4 based composite photocatalysts have been reported. A number of semiconductors, such as WO_3 [25], ZnO [26], $SmVO_4$ [27], Bi_2WO_6 [28], AgBr [29] etc., have been used as a doper to strengthen the photocatalytic activity of g-C_3N_4. The promotion effect was usually explained by three different mechanisms. The first one is sensitization in which electrons generated by visible-light irradiation in g-C_3N_4 migrate to a wider bandgap semiconductor (such as ZnO, TiO_2, YVO_4) [26,30-31], while the photogenerated holes stay in the g-C_3N_4. This would facilitate electron–hole separation, suppress charge recombination, and hence improve the photocatalytic activity. The second one is often-associated with heterojunction composite photocatalyst in which both semiconductors can be excited to generate electron–hole pairs [27-28]. The photogenerated electrons from g-C_3N_4 with a higher conduction band could transport to another semiconductor with a lower conduction band. Meanwhile, the photogenerated holes from the semiconductor with a lower valence band transport to the g-C_3N_4 with a higher valence band. The double charge

transfer may also lead to the separation of electrons and holes and enhance the photo-catalytic efficiency. The third one could be called as direct Z-scheme type mechanism. Taking g-C_3N_4/$TiO_{2-x}S_x$ photocatalyst as an example, the photogenerated electrons from the $TiO_{2-x}S_x$ semiconductor with a lower conduction band recombine with photogenerated holes from the g-C_3N_4 with a higher valance band [32]. By this way, the electrons on g-C_3N_4 and holes on S-TiO_2 are separated efficiently. The g-C_3N_4/$TiO_{2-x}S_x$ composite showed four times higher quantum efficiency than S doped TiO_2 in the photodegrdation of acetaldehyde [32]. Although all the three mechanisms have been widely used by scientists to explain their works, there are still some questions about how to choose the mechanism suitable to a specific research. The band edge potential of semiconductor is generally considered as the criterion which works well in the differentiation of the first two mechanisms. However, it is not enough to distinguish the double-charge-transfer mechanism and direct Z-scheme mechanism. More detailed works need to be done for resolving the issue.

A new Z-scheme type photocatalyst, MoO_3/g-C_3N_4 composite in spite of its similarity to g-C_3N_4 doped MoO_3 composite [33], was developed in this paper. Li et al. [33] think that the g-C_3N_4/MoO_3 composite follows the double-charge-transfer mechanism. However, this research proved that the real mechanism is Z-scheme type mechanism based on the active species trapping experiment. In addition, in comparison to Li's catalyst with 93.0 wt.% MoO_3, a very low content of MoO_3 (1.5wt%) was used in this work, while the latter exhibits excellent photocatalytic activity in dyes photodegradation under visible light irradiation. The high activity and low cost indicates that the MoO_3/g-C_3N_4 is promising photocatalyst.

2. Experimental Section

2.1 Catalysts preparation

$(NH_4)_6Mo_7O_{24}{\cdot}4H_2O$ (>99.0%), melamine (99.0%), urea (99.0%), tetrabutyl titanate (>99.0%), benzoquinone (>98.0%), KI (>99.0%), isopropanol (>99.7%), coumarin (>99.0%), and ethanol (>99.5%) were purchased and used without further purification. N-doped TiO_2 was prepared by a modified sol-gel method [34]. Pure MoO_3 was prepared by directly calcining at 500 ^oC for 4 h. Pure g-C_3N_4 powders were prepared by directly calcining melamine in a muffle furnace. In a typical synthesis run, 6 g of melamine was placed in an alumina crucible with a cover. The crucible was heated to 520 ^oC for 4 h at a heating rate of 10 ^oC/min. After cooling to room temperature, yellow g-C_3N_4 was obtained in a powder form.

The MoO_3/g-C_3N_4 composites were prepared according to the following procedure. 0.03 g of MoO_3 and 1.97 g of g-C_3N_4 were mixed and ground in an agate mortar for 20 min. Then, the mixture was calcined at 400 ^oC for 2h to obtain the 1.5wt.% MoO_3/g-C_3N_4 catalyst. Other MoO_3/g-C_3N_4 catalysts were prepared by a same method except the g-C_3N_4 concentration.

2.2 Photocatalyic reaction

The photocatalytic activities of the synthesized powders were evaluated by degrading methyl orange (MO) under visible-light irradiation. The light source for photocatalysis was a spherical Xe lamp (350 W). Two optical filters were used to eliminate the UV light and infrared light (800 nm > λ > 420 nm). The power density at the position of reactor is about 16 mW/cm^2. The volume of initial MO solution is 100 mL. All the powder contents in the MO aqueous solution are 0.10 g/100mL. Prior to irradiation, the mixture was agitated for an hour to ensure adsorption/desorption equilibrium at room temperature. At regular intervals, samples were withdrawn and centrifuged to remove photocatalyst for analysis. The concentration of aqueous MO was determined by measuring its absorbance at the range of 400 nm to 700 nm. The MO degradation was calculated by Lambert–Beer equation. Photoactivity for MO under visible-light irradiation in the absence of the photocatalyst was also evaluated. The photodegration of other dyes, rodamine B (RhB) and methylene blue (MB), was also carried out by the similar procedure.

The examination experiment process of reactive species was similar to the photodegradation experiment. A quantity of scavengers was introduced into the MO solution prior to addition of the catalyst. The concentration of scavengers was controlled to be 0.01 mol/L according to the previous studies [35-36] with the exception of benzoquinone (0.0001 mol/L).

The formation rate of •OH at photo-illuminated sample/water interface was detected by the photoluminescence (PL) technique using coumarin (COU) as a probe molecule. The measurement was carried out in the photocatalytic testing system. In a typical run, 0.2 g of the samples was added to an aqueous solution (100 mL) containing 10 mM COU in a 250 mL beaker. After irradiation for a given time, 8 mL aliquots were sampled and centrifuged for analysis. The •OH formed in the system can react with COU and generate 7-hydroxycoumarin (7HC), the fluorescence intensity of which is directly proportional to the generated •OH [37].

2.3 Characterization

Thermogravimetry analysis (TG-DTA; Netzsch STA449) was carried out in a flow of air (10 mL/min) at a heating rate of 10 ^oC/min. The specific surface areas were measured on Autosorb-1 (Quantachrome Instruments) with Brunauer–Emmett–Teller (BET) method. The XRD characterization of catalysts was carried out on Philips PW3040/60 X-ray diffractometer, using Cu Kα radiation (40 kV/40 mA). The FT-IR spectra of the catalysts were recorded on Nicolet NEXUS670 with a resolution of 4 cm^{-1}. The X-ray photoelectron spectroscopy (XPS) measurements were performed with a Quantum 2000 Scanning ESCA Microprobe instrument using AlKα. The C 1s signal was set to a position of 284.6 eV. The scanning electron microscopy (SEM) pictures were taken on a field emission scanning electron microscope (LEO-1530). The TEM images were collected with a JEM-2010F transmission electron microscope at an accelerating voltage of 200 kV. The DRS spectra of catalysts were recorded on a UV-vis spectrometer (PerkinElmer Lambda900) equipped with an integrating sphere. The PL spectra were collected on FLS-920 spectrometer (Edinburgh Instrument), using a Xe lamp (excitation at 365 nm and 332 nm for photocatalyst and 7HC, respectively) as light source.

Photocurrent was measured on an electrochemical analyzer (CHI660B) in a two-electrode system under zero bias. The

prepared sample and a Pt wire are used as the working electrode and the counter electrode, respectively. A 350 W Xe arc lamp through a UV-cutoff filter (λ>420 nm) served as a light source. Na_2SO_4 (0.5 mol/L) aqueous solution was used as the electrolyte. Working electrodes were prepared based on the literature reported [27].

3. Results and discussion

3.1 Characterizations of g-C_3N_4, MoO_3 and MoO_3/g-C_3N_4 composites.

Thermo-gravimetric analysis was performed from room temperature to 800 °C under air conditions to determine the real content of MoO_3 in MoO_3/g-C_3N_4 composite. The results are shown in Fig. 1. For clarity, only the TG profiles of pure g-C_3N_4 and three MoO_3/g-C_3N_4 composites are presented. It can be observed that the weight of pure g-C_3N_4 decreased rapidly in the temperature range of 600-750 °C, indicating that the decomposition of g-C_3N_4 occurred in this temperature range. For MoO_3/g-C_3N_4 composite, the weight-loss range shift forwards to 480-570 °C, which suggests that the existence of MoO_3 promotes the combustion of g-C_3N_4, as observed in the $SmVO_4$/g-C_3N_4 photocatalyst [27]. The real concentration of MoO_3 can be easily calculated from the residuals after the samples were heated over 600 °C. As shown in Table 1, the real MoO_3 content is slightly larger than the theoretical values. Actually, the difference between the real and theoretical value of g-C_3N_4 is usually large in the reported g-C_3N_4 based photocatalysts [27,38-39]. The small difference in the MoO_3/g-C_3N_4 might be ascribed to the low preparation temperature (400 °C). Besides the weight loss of g-C_3N_4, another weight loss between 750-800 °C in the MoO_3/g-C_3N_4 composites, could be ascribed to the vaporization of MoO_3. This result is consistent with the phase composition. The BET surface areas of MoO_3/g-C_3N_4 composites are also shown in Table 1. Pure MoO_3 exhibits much lower surface area than pure g-C_3N_4. However, the addition of a small amount of MoO_3 to g-C_3N_4 led to the increase in the BET value of photocatalyst, which might be due to the interaction between the two semiconductors. With the further increase of the MoO_3 concentration, the BET value decreased from 14.7 m^2/g to 6.9 m^2/g. 15 wt.% MoO_3/g-C_3N_4 sample presents the lowest specific surface area.

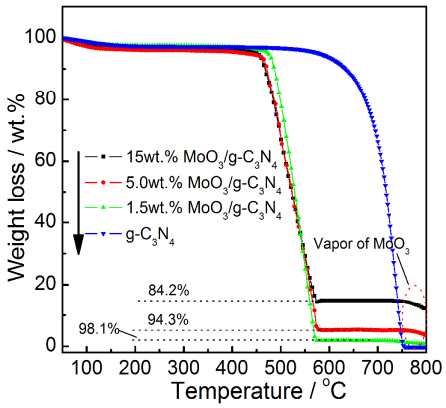

Fig. 1 TG profiles of MoO_3/g-C_3N_4 composites.

Table 1 Specific surface area and the real MoO_3 concentrations of MoO_3/g-C_3N_4 composites.

Catalysts	S/$m^2 \cdot g^{-1}$	MoO_3 content/ wt.%
g-C_3N_4	13	0
MoO_3	1.7	100
1.0 wt.% MoO_3/g-C_3N_4	14.7	1.2
1.5wt.% MoO_3/g-C_3N_4	14.4	1.9
2.0wt.% MoO_3/g-C_3N_4	11.6	2.4
5.0wt.% MoO_3/g-C_3N_4	7.1	5.7
15wt.% MoO_3/g-C_3N_4	6.9	15.8

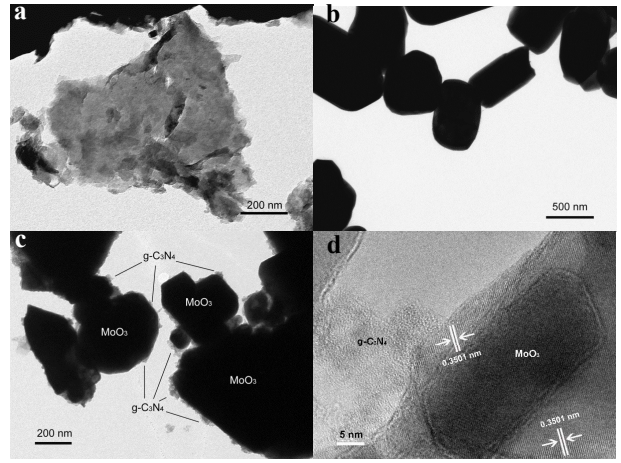

Fig. 2 TEM images of g-C_3N_4 (a), MoO_3 (b), and1.5 wt.% MoO_3/g-C_3N_4 (c,d) photocatalysts.

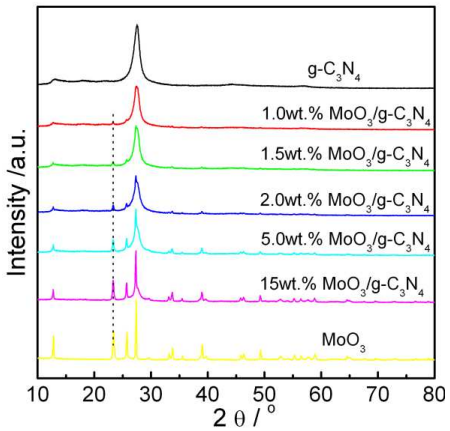

Fig. 3 XRD patterns of MoO_3/g-C_3N_4 composites with different MoO_3 concentration.

Fig. 2 shows the TEM pictures of g-C_3N_4, MoO_3, and 1.5 wt.% MoO_3/g-C_3N_4 composite. As shown in Fig. 2a, the morphology of pure g-C_3N_4 seems to be smooth, which is also confirmed by SEM observation (Fig. S2a). The layer structure might be the origin of the special morphology of g-C_3N_4. Different from g-C_3N_4, MoO_3 sample had a particle size of 200-600 nm, and a grain-like morphology with polygonal grain shapes (Fig. 2b and S2b). For the MoO_3/g-C_3N_4 composite, several MoO_3 particles were sparsely observed on the g-C_3N_4 surface (Fig. S2c), and almost all particles were in direct contact with the g-C_3N_4. The TEM image of MoO_3/g-C_3N_4 gives detailed information on the contact of the two semiconductors. As can be seen in Fig. 2c, the big black particles could be assigned to MoO_3 grain, while g-C_3N_4 closely adhered to the surface of MoO_3. The close contact can be observed more clearly in the high-resolution TEM image. As shown in Fig. 2d, two different phases were observed. The dark and big phase which exhibits fringes with an interplanar spacing of about 0.3501 nm can be indexed into the

(040) plane of MoO_3, whereas another phase without fringes can be assigned to g-C_3N_4. Additionally, because the MoO_3/g-C_3N_4 hybrids were ultrasonicated for 20 min before TEM analysis, the result in Fig. 2c and 2d indicates that the interaction between the MoO_3 particles and g-C_3N_4 is very strong, which is beneficial to the formation of hetero-junction of MoO_3 and g-C_3N_4.

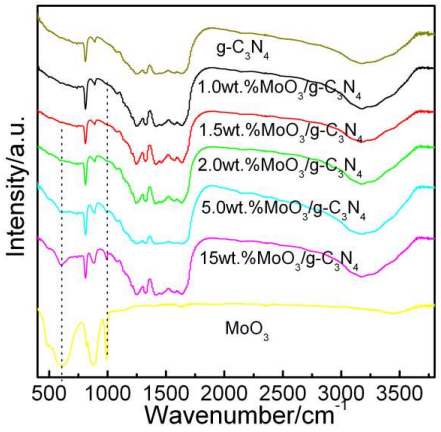

Fig. 4 FT-IR spectra of MoO_3/g-C_3N_4 composites with different MoO_3 concentration.

The structure of MoO_3/g-C_3N_4 composites was characterized by XRD and FT-IR. Fig. 3 shows the XRD patterns of MoO_3, g-C_3N_4, and MoO_3/g-C_3N_4 composites with different MoO_3 concentration. Pure g-C_3N_4 shows two broad peaks at 2θ= 13.0 ° and 27.4°, which are the (001) and (002) diffraction planes of the graphite-like carbon nitride, respectively [13]. Pure MoO_3 is in its orthorhombic phase (JCPDF 35-0609) and exhibits several strong diffraction peaks at 2θ = 12.8 °, 23.4 °, 25.7 °, 27.3 °, 33.8 °, 39.0 ° [40]. In the MoO_3/g-C_3N_4 composite, although the content of MoO_3 is very low, MoO_3 phase could still be observed due to its strong XRD signal. As MoO_3 concentration increases from 1.0 wt% to 15 wt.%, the diffraction peaks of MoO_3 are gradually intensified, whereas the peaks of g-C_3N_4 are weakened. This result accords well with that of TG experiment. With the exception of MoO_3 and g-C_3N_4, no other phase was observed. The same result was also obtained in the FT-IR experiment. As shown in Fig. 4, pure g-C_3N_4 shows strong IR signal in the range of 1200-1600 cm^{-1}, which could be assigned to the C=N and aromatic C-N stretching vibration modes [41]. In addition, the signal of out-of plane bending modes of C-N heterocycle was also observed at 808 cm^{-1} [41]. For MoO_3, only three strong IR peaks were observed. The peak at 996 cm^{-1} could be assigned to the Mo=O stretching mode, while the peaks at 562 cm^{-1} and 859 cm^{-1} originate from the stretching mode of oxygen linked with three metal atoms and in the Mo-O-Mo units, respectively [42]. In the case of MoO_3/g-C_3N_4 composite, the position of these characteristic peaks is as same as that of pure phase. The peak intensity of MoO_3 increases with the MoO_3 content, which is consistent with the results obtained with XRD.

XPS measurements were performed to explicate the valence states of various species. Fig. 5 shows the C1s high resolution XPS spectra of MoO_3, g-C_3N_4 and several MoO_3/g-C_3N_4 composites. Pure g-C_3N_4 has two C1s peak located at 284.6 eV and 288.0 eV, which could be attributed to C-C coordination of carbon-containing contaminations and N-C-N coordination in graphitic carbon nitride, respectively [41]. For MoO_3, only the contaminated carbon was observed. Hence, the C1s peak at 288.0 eV could be used to verify the existence of g-C_3N_4 in the MoO_3/g-C_3N_4 photocatalyst. Generally, the N1s peak can also be the standard. The peak at 398.5 eV and 400.6 eV could be separately assigned to the nitrogen atoms in C-N-C and -NH_x groups [41]. No shift was observed in the C1s or N1s peak after the addition of MoO_3 except a slight red shift of N1s in 15wt.% MoO_3/g-C_3N_4 sample. Li et al. observed the shift of N1s peak in 7 wt.% g-C_3N_4/MoO_3 composite and attributed it to the interaction between Mo and N atoms [33]. However, it should be noted that the binding energy (BE) of Mo $3p_{3/2}$ is very close to that of N1s. We think the contribution of Mo $3p_{3/2}$ might be the reason of the N1s peak shift. Fig. 5c shows the high resolution XPS peak of O1s. MoO_3 has a strong O1s peak at 530.8 eV which could be attributed to the O^{2-} in molybdenum oxide [43], while g-C_3N_4 has a small O1s peak originated from adsorbed H_2O [41]. The O1s peak of MoO_3/g-C_3N_4 could be seen as the overlap of the two oxygen species. With the increase of the MoO_3 content, the position of O1s shifts to low binding energy end. The high-resolution XPS spectrum of Mo 3d exhibits the Mo ($3d_{5/2}$, $3d_{3/2}$) doublet at 232.9 eV and 236.0 eV (Fig. 5d), the typical binding energies of Mo^{6+} [44-45]. In the case of MoO_3/g-C_3N_4, the BEs of $Mo3d_{5/2}$ and $Mo3d_{3/2}$ are 232.3 and 235.4 eV, respectively. Earlier studies show that the Mo $3d_{5/2}$ BE of MoO_2 is 229.6 eV, and the BE of Mo^{5+} $3d_{5/2}$ is 232.0 eV [44-45]. So, both Mo^{5+} and Mo^{6+} exist in the surface of MoO_3/g-C_3N_4 samples, although the XRD experiment indicates that molybdenum exists in the forms of crystalline MoO_3. The Mo^{5+} might originate from the catalytic oxidation of g-C_3N_4 by MoO_3 during the preparation of MoO_3/g-C_3N_4, which has been proven by the TG-DTA experiment (see Fig. S1). Some Mo^{6+} ions were reduced to Mo^{5+} during the heating process. The reaction between g-C_3N_4 and MoO_3 consumed some g-C_3N_4. Meanwhile, it promotes the interaction between the two semiconductors, which benefits the decrease in interface energy and the charge transfer between them. In addition, it could be observed that the change in MoO_3 concentration did not affect the BE of $Mo3d_{5/2}$, which suggests that the surface Mo^{5+} concentration is stable in the MoO_3/g-C_3N_4 composites. The surface phase composition of the 1.5 wt% MoO_3/g-C_3N_4 sample was obtained based on the XPS spectra. The MoO_3 concentration of the sample (Table S1) is 1.0 mol%, which is close to 1.2 mol% (obtained with TG). This result

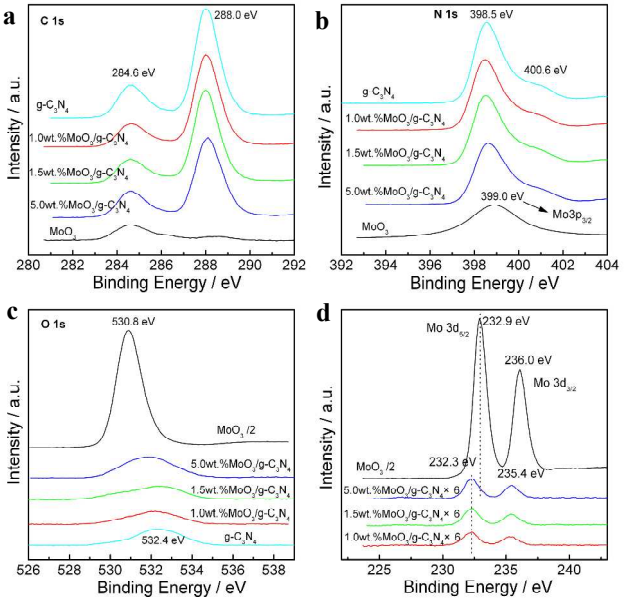

Fig. 5 XPS spectra of MoO_3, g-C_3N_4 and MoO_3/g-C_3N_4 composites, (a) C1s; (b) N1s; (c) O1s; (d) Mo3d.

indicates well dispersion of MoO_3 in composite, benefiting the formation of heterojunction structure between MoO_3 and g-C_3N_4. The valence band (VB) XPS spectra of g-C_3N_4 and MoO_3 are shown in Fig. 6. The position of the valence band edges of g-C_3N_4 and MoO_3 are 1.53 eV and 3.20 eV, respectively.

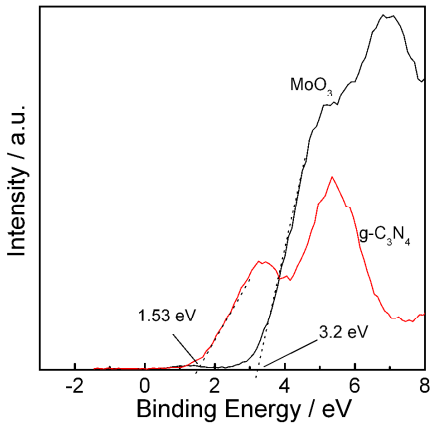

Fig. 6 Valence band XPS of MoO_3 and g-C_3N_4

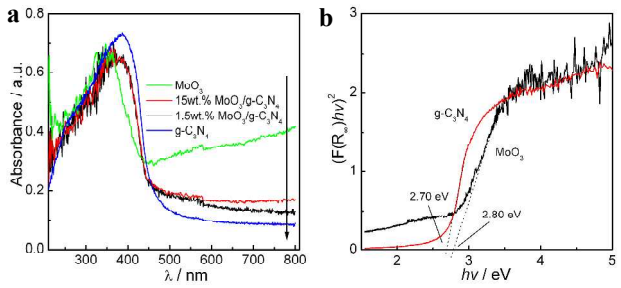

Fig. 7 UV-vis spectra of MoO_3/g-C_3N_4 (a) composites and the estimated band gaps of g-C_3N_4 and MoO_3 (b).

Fig. 7 shows the UV-vis DRS spectra of MoO_3/g-C_3N_4 composites. Only the spectra of 1.5wt.% MoO_3/g-C_3N_4 and 15wt.% MoO_3/g-C_3N_4 photocatalysts are presented. For all samples, the optical absorption edge was estimated to be at around 470 nm. This is consistent with their pale yellow color. Pure g-C_3N_4 has the best photoabsorption performance. The band gap was estimated to be 2.70 eV based on the K-M equation [46]. The band gap of MoO_3 is 2.80 eV. Both accord well with the reported values [13,45]. The optical properties of MoO_3/g-C_3N_4 fall in between those of MoO_3 and g-C_3N_4. However, due to the low concentration of MoO_3 and the similar band gap of the two semiconductors, the composites with different MoO_3 contents exhibit nearly same photoabsorption performance

3.2 Photocatalytic activities of g-C_3N_4, MoO_3, and MoO_3/g-C_3N_4.

To evaluate the photocatalytic activity of as-prepared MoO_3/g-C_3N_4 composites, the degradation of MO was carried out. Fig. 8a displays the changes of the MO concentration versus the reaction time over MoO_3/g-C_3N_4 photocatalysts prepared with different MoO_3 concentrations. The blank test shows that MO is stable under visible light irradiation, indicating that the photolysis of MO is negligible. MoO_3 barely shows activity for MO photodegradation, while g-C_3N_4 demonstrates good photocatalytic activity with a degradation rate of 0.0017 min^{-1} (Fig. 8b). The rate was estimated based on

$$\ln(C_0/C_t)=kt \qquad \text{(E1)}$$

where C_0 is the equilibrium concentration of MO after 60 min dark adsorption, C_t is the MO concentration remaining in the solution at irradiation time t (min), and k is the observed rate constant [28-29]. The addition of MoO_3 to g-C_3N_4 promotes the degradation of MO effectively. With the increase in MoO_3 concentration, the photocatalytic activity of MoO_3/g-C_3N_4 increases and then decreases. 1.5wt.% MoO_3/g-C_3N_4 exhibits the highest photocatalytic efficiency. The k value is 0.0177 min^{-1} which is 10.4 times higher than that of pure g-C_3N_4. Obviously, the coupling of MoO_3 and g-C_3N_4 creates an excellent composite photocatalyst. Considering that the MoO_3/g-C_3N_4 composites have similar specific surface area with g-C_3N_4, the enhanced photoactivity may be ascribed to the improvement in charge transmission between the semiconductors g-C_3N_4 and MoO_3 prolonged the lifetime of charge carriers. Moreover, the photoactivity of the coupled semiconductors was also affected by the surface contact between particles. 1.5wt.% MoO_3/g-C_3N_4 might have the highest contact interfaces between MoO_3 and g-C_3N_4, and thus the highest photocatalytic efficiency.

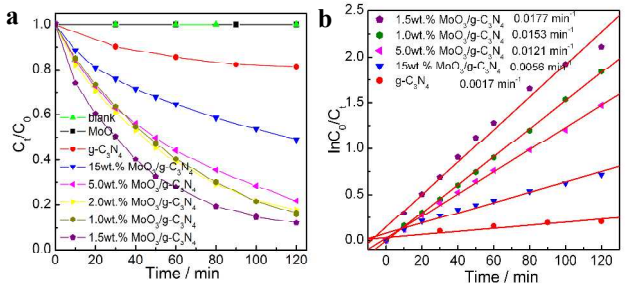

Fig. 8 Photocatalytic activities of MoO_3/g-C_3N_4 composites on photodegradation of MO under visible-light irradiation (a) and the corresponding kinetic studies (b). (Catalyst's content: 1.0g/L; MO content: 20 ppm).

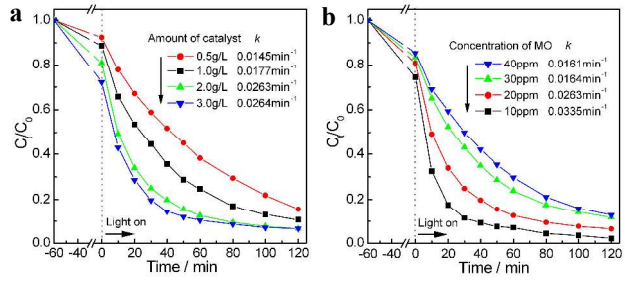

Fig. 9 Effect of catalyst content (a) and initial dye concentration (b) on the degradation of MO.

Reaction conditions also have great effects on the photocatalytic reaction. The optimal reaction condition could accelerate the photocataltyic oxidation of dye. Therefore, in order to degrade MO more efficiently, the 1.5 wt.% MoO_3/g-C_3N_4 sample was employed for the following investigations. It can be seen from Fig. 9a that the degradation rate of MO increased from 0.0145 min^{-1} to 0.0210 min^{-1} with catalyst amount, and then decreased slightly. Higher catalyst amount means higher availability of total surface area and active sites of the catalyst, and thus better adsorption of MO and degradation rate. However, when the catalyst is overdosed, the reductions in light penetration

and light scattering would result in a reduction of degradation rate. An optimal amount (2.0 g/L) was chosen for the further study. Fig. 9b shows the effect of the initial concentration of MO on the photocatalytic degradation of MO over 1.5 wt.% MoO_3/g-C_3N_4 composite. The increase in MO concentration reduces the degradation efficiency, which might be due to the light attenuation in MO solution or the visible light screening effect of the dye. The higher the MO concentration is, the fewer the light could pass through the MO solution and reach the photocatalyst, and lead to lower photoactivity.

The influence of the pH on the photocatalytic degradation of MO was also investigated and the results are shown in Fig. 10a. When the pH value was lower than 9, pH had little effect on the photocatalytic oxidation of MO. The 1.5 wt.% MoO_3/g-C_3N_4 photocatalyst exhibited good photoactivity in both neutral and acid solution. However, when pH was higher than 9, the photocatalytic activity decreased considerably. The loss of MoO_3 might result in the decrease in photoactivity, which was also observed in cyclic experiments. As shown in Fig. 10b, the degradation efficiency of 1.5 wt.% MoO_3/g-C_3N_4 composite decreased gradually with the increase in the number of cyclic test. In the fourth run, only 55 % of the initial activity was obtained. According to the results of XRD experiments, the disappearance of MoO_3 phase might lead to the inactivation of the photocatalyst (Fig. S2). Unlike WO_3, MoO_3 has very low solubility in water (4.9 g/L, 28 ^oC). Although the strong interaction between g-C_3N_4 and MoO_3 might slow down the dissolution process, the inactivation of the MoO_3/g-C_3N_4 is observed. It should be noted that the inactivation of MoO_3-containing photocatalyst has not been reported before. All researchers claimed that the synthesized MoO_3-containing photocatalyst is stable and can be recycled with water purification [32,33,47-48]. The observation might result from the high concentration of MoO_3 in those photocatalysts. MoO_3 dissolution did not affect photocatalytic activity during the several cyclic tests. However, it is no doubt that the inactivation of MoO_3-containing photocatalyst during water purification is unavoidable due to the solubility of MoO_3. The MoO_3-containing composites are more suitable for air purification such as the photodegradation of acetone with SO_4^{2-}/MoO_3/MgF_2 composite [41].

Fig. 11a shows the photocatalytic activity of MO, MB, and RhB in the presence of 1.5wt.%MoO_3/g-C_3N_4 composite. It can be seen that the MB and RhB dyes can also be photodegraded efficiently over the MoO_3/g-C_3N_4 photocatalyst besides MO. Indeed, many photocatalysts could only degrade one type of dye. For example, it was reported that $CaBi_6O_{10}$/Bi_2O_3 photocatalyst is only effective in RhB photodegradation [34]. Yan et al. found that pure g-C_3N_4 exhibited much higher photocatalytic activity in RhB degradation than that in MO degradation [49]. The result in Fig. 11a indicates the general applicability of the synthesized MoO_3/g-C_3N_4 photocatalyst since RhB and MO are two different type of dyes. Fig. 11b displays the photocatalytic activities of different photocatalysts in photodegradation of MO. Actually, the g-C_3N_4/MoO_3 and WO_3/g-C_3N_4 composite photocatalysts were also prepared based on the reported literatures [25,33]. However, the synthesized photocatalysts display different photocatalytic behavior from the literatures, which might be due to the inconsistence in preparation techniques and experimental conditions. Hence, in order to eliminate their effects, only the N-TiO_2 [34], $DyVO_4$/g-C_3N_4 [38], and YVO_4/g-C_3N_4 [31] photocatalysts which we have previously reported were chosen as the reference photocatalysts. The result shown in Fig. 11b demonstrated the superiority of MoO_3/g-C_3N_4 composite. The MoO_3/g-C_3N_4 photocatalyst had better performance on photocatalytic oxidation of MO than the other g-C_3N_4 based photocatlaysts.

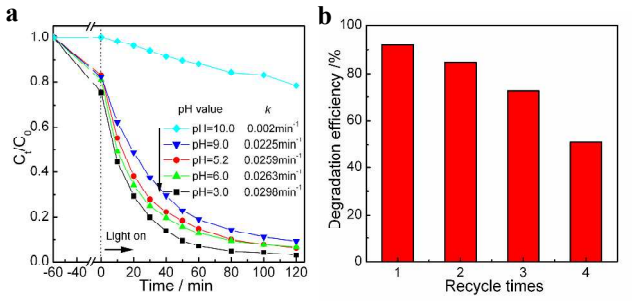

Fig. 10 Effect of the pH value of MO solution on the degradation of MO (a) and the cycling run of 1.5wt.% MoO_3/g-C_3N_4 (b). (content of catalyst: 2.0g/L; content of MO: 20 ppm).

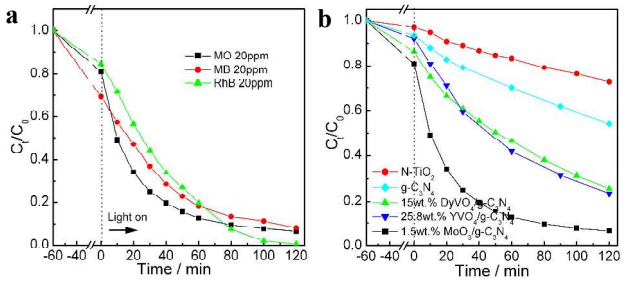

Fig. 11 The photodegradation of different organics over 1.5wt.%MoO_3/g-C_3N_4 sample (a) and the photodegration of MO over different photocatalysts (b). (Content of catalyst: 2.0g/L; pH=6.0).

Therefore, the synthesized MoO_3/g-C_3N_4 composite is an excellent photocatalyst for the photodegradation of MO, RhB, and MB. The addition of a small amount of MoO_3 could greatly promote the photocatalytic activity of g-C_3N_4. The highest photocatalytic activity could be obtained by optimizing the influencing factors (MoO_3 concentration, catalyst amount, initial MO concentration, pH of MO solution). However, MoO_3/g-C_3N_4 composite is not stable in water. In order to make it applicable for water purification, the modification should be done, which includes coating the exposed MoO_3 surface with a nanocarbon layer to prevent the dissolution of MoO_3.

3.3 Possible mechanism of enhanced photocatalytic activity of MoO_3/g-C_3N_4 composite

Although the surface area of a photocatalyst has been considered as an important factor in determining the photocatalytic activity, the separation efficiency of electron-hole pairs of the composite photocatalyst including MoO_3/g-C_3N_4 used in this research is always the key factor. The excellent photocatalytic activity is associated with the enhanced separation efficiency resulting from the addition of MoO_3. XPS experiment shows that some Mo^{5+} species formed on the surface of the composite might contribute to the separation of electron-hole pairs because Mo^{5+} has been reported to be the low trap of hole [7,45]. However, due to the inconsistency of surface Mo^{5+} content and photoactivity, the coupling effect between MoO_3 and g-C_3N_4 should be the main reason, suppressing the recombination of electron-hole pairs, and subsequently improving the photocatalytic efficiency. The PL experiment was carried out to confirm the assumption. Fig. 12 shows the PL spectra of pure g-C_3N_4, 1.5 wt.% MoO_3/g-C_3N_4 composite, and 1.9wt.% MoO_3/g-C_3N_4 mixture. The mixture containing the same amount of MoO_3 as the 1.5 wt.% MoO_3/g-C_3N_4 sample was prepared as a reference catalyst. G-C_3N_4 has a

strong PL emission at about 460 nm, an indication of rapid recombination of electrons and holes [50]. The other two samples have a PL peak at the same position. The peak intensities of three materials are in the order of g-C_3N_4 >1.9 wt.% MoO_3/g-C_3N_4 mixture > 1.5 wt.% MoO_3/g-C_3N_4 composite. In general, the surface energies of MoO_3 and g-C_3N_4 in the mixture should be high due to the lack of calcination, which retards the interparticle electron transfer. Hence, the weak PL intensity of 1.9 wt.% MoO_3/g-C_3N_4 mixture could be mainly ascribed to the decrease in g-C_3N_4 concentration. The fact that PL peak of the 1.5 wt.% MoO_3/g-C_3N_4 composite is weaker than that of the physical mixture verifies the existence of the charge transfer between MoO_3 and g-C_3N_4 particles.

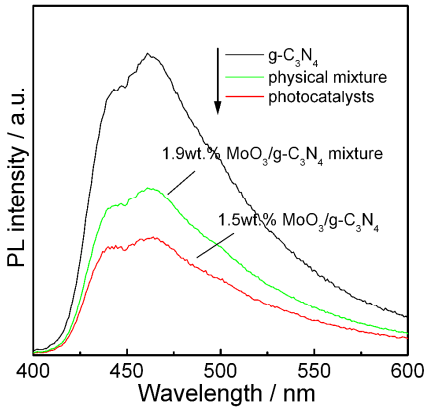

Fig. 12 Photoluminescence spectra of pure g-C_3N_4, 1.5 wt.% MoO_3/g-C_3N_4 composite, and 1.9wt.% MoO_3/g-C_3N_4 physical mixture.

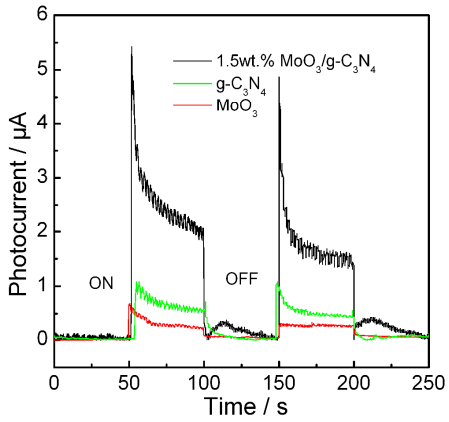

Fig. 13 Transient photocurrent responses for g-C_3N_4 and 1.5wt.% MoO_3/g-C_3N_4 photocatalysts.

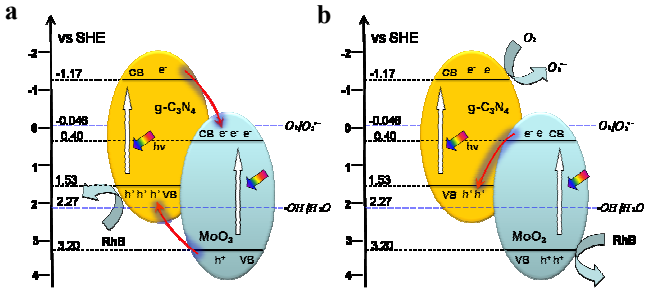

Fig. 14 Possible schemes for electron–hole separation and transport at the visible-light-driven MoO_3/g-C_3N_4 composite interface: (a) double charge transfer mechanism, (b) Z-Scheme mechanism.

The PT experiments were also carried out to reveal dynamics of the charge transfer between the interfacial surface of MoO_3 and g-C_3N_4 semiconductors. As shown from Fig. 13, the photocurrent of 1.5 wt.% MoO_3/g-C_3N_4 is much higher than that of g-C_3N_4 or MoO_3, thus holds stronger ability in generating and transferring the photoexcited charge carrier under visible light irradiation [51,52]. The results in Fig. 13 are well in agreement with those from the PL experiments.

Therefore, it is obvious that the efficient charge separation is the origin of the high photoactivity of MoO_3/g-C_3N_4. However, the associated mechanism is unclear. Based on

$$E_{cb}=E_g-E_{vb} \quad (E2)$$

and the results of VB XPS and DRS, the band edge potentials of MoO_3 and g-C_3N_4 could be determined. The sensitization mechanism should be excluded since both MoO_3 and g-C_3N_4 have visible light absorption ability. However, the final determination of the working mechanism of the MoO_3/g-C_3N_4 photocatalyst is still difficult because the band potentials of MoO_3 and g-C_3N_4 meet the requirements of both mechanisms (Fig. 14). Li et al. reported that g-C_3N_4/MoO_3 composite follows the double charge transfer mechanism (Fig. 14a) [33]. This mechanism was also thought to work in another similar photocatalyst, WO_3/g-C_3N_4 composite [25,53]. But these authors did not consider the possibility of Z-scheme type mechanism. Meanwhile, some studies showed that the photogenerated electrons migrate by the Z-scheme route in the MoO_3-containing composite photocatalysts (MoO_3/$TiO_{2-x}S_x$ [32], Pt/MoO_3/TiO_2 [54], MoO_3/TiO_2 [55]). The theory is based on the assumption that the photocatalytic efficiency of the Z-scheme photocatalysis system is limited by the semiconductor with a wider band gap [56]. However, due to the similarity band gaps of MoO_3 and g-C_3N_4, a new method is needed to determine the function mechanism of MoO_3/g-C_3N_4.

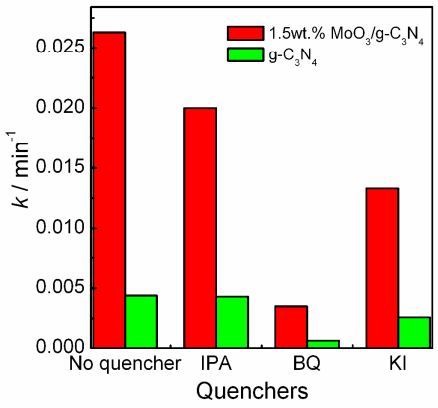

Fig. 15 Kinetic constants of g-C_3N_4 and 1.5 wt.% MoO_3/g-C_3N_4 photocatalyst with different quenchers.

The activity of a photocatalyst originates from the redox ability of electrons and holes [1-2]. The band potentials of a semiconductor greatly affect the photocatalytic reaction. Actually, band potential difference was considered as an important reason of the higher photoactivities of BiOCl and Zn_2GeO_4 than that of P25 [57-58]. However, for composite photocatalysts, the positive effect of charge separation is great enough to control the photocatalytic reaction. The effect of the change in redox ability resulting from the charge migration is usually neglected. Migration does influence the process of the photocatalytic oxidation of organics. For example, although the photocatalytic activity of g-C_3N_4 was greatly improved due to the addition of $GdVO_4$, the •OH concentration in the presence of

$GdVO_4$/g-C_3N_4 composite is lower than that of pure g-C_3N_4 and $GdVO_4$ [59]. This change in the content of reactive species could be attributed to the decrease in redox potentials of electron and holes. Hence, in the case of MoO_3/g-C_3N_4 composite, the change in redox ability can affect the reactive species. If the MoO_3/g-C_3N_4 photocatalyst follows the same mechanism as $GdVO_4$/g-C_3N_4 composite (double charge transfer mechanism, Fig. 14 a), the decrease in •OH concentration would be observed over MoO_3/g-C_3N_4 composite. In addition, due to the conduction band potential of MoO_3 is lower than the standard reduction potential of $•O_2^-/O_2$, the electron transfer from the CB of g-C_3N_4 to that of MoO_3 would lead to the significant decrease in $•O_2^-$ concentration. It would be impossible that the MoO_3/g-C_3N_4 composite and pure g-C_3N_4 have the same dominant reactive species $•O_2^-$. On the contrary, if the MoO_3/g-C_3N_4 follows the Z-scheme type mechanism, the opposite result would be obtained.

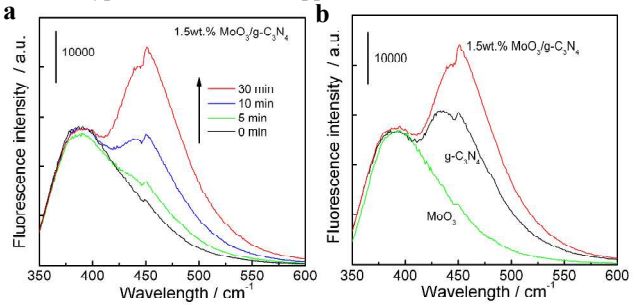

Fig. 16 •OH-trapping photoluminescence spectra of photocatalyst under visible-light irradiation in a solution of COU at room temperature (a) 1.5 wt.% MoO_3/g-C_3N_4. (b) MoO_3, g-C_3N_4, and 1.5 wt.% MoO_3/g-C_3N_4 samples under light irradiation for 30 min.

Fig. 15 shows the kinetic constants of g-C_3N_4 and 1.5 wt.% MoO_3/g-C_3N_4 photocatalyst in the presence of different quenchers. The addition of benzoquinone (BQ, $•O_2^-$ scavenger) greatly decreased the photocatalyic activity of g-C_3N_4, indicating that $•O_2^-$ is the dominant active species [35,36], which is also consistent with the Ji's work [60]. A small decrease in *k* was also observed after the addition of KI (KI, •OH and h^+ scavenger) [35,36], whereas isopropanol (IPA, a quencher of •OH) has nearly no effect on the degradation of MO in the presence of g-C_3N_4 catalyst [35,36]. For the MoO_3/g-C_3N_4 composite, similar results were obtained. The active trapping experiments verified that $•O_2^-$ and h^+ are the reactive species during the photocatalytic oxidation of MO. Thus, MoO_3/g-C_3N_4 composite photocatalyst follows the direct Z-scheme type mechanism. Besides, it could be noted that the isopropanol scavenger displayed a stronger effect on the photoactivity of MoO_3/g-C_3N_4 than that of g-C_3N_4. This phenomenon suggests the increase in •OH concentration in the MoO_3/g-C_3N_4 composite, which is in a good agreement with the expectation of the Z-scheme mechanism.

The increased •OH concentration was verified via the experiments with the trapping of hydroxyl radicals (•OH) by COU. Fig. 16a displays the •OH-trapping photoluminescence spectra of 1.5 wt.% MoO_3/g-C_3N_4 composite under visible-light irradiation. PL emission peak at approximately 456 nm was observed and gradually increased with prolonged irradiation time, which indicates that the •OH was photogenerated [37]. The PL spectra of MoO_3, g-C_3N_4 and 1.5 wt.% MoO_3/g-C_3N_4 samples under visible light irradiation for 30 min are shown in Fig. 16b. The 1.5 wt.% MoO_3/g-C_3N_4 sample has the strongest PL peak, indicating that •OH concentration was higher than that of pure g-C_3N_4. Obviously, due to the high concentrations of the electron on the CB of g-C_3N_4 and holes on the VB of MoO_3, and thus ease in the generation of •OH species. The data in Fig. 15 and 16 clearly verifies that Z-scheme type mechanism is applicable to the MoO_3/g-C_3N_4 composite photocatalyst.

4. Conclusion

The prepared MoO_3/g-C_3N_4 powders exhibited excellent performance in the degradation of MO, RhB and MB, and displayed much higher photocatalytic activity than single g-C_3N_4 or MoO_3 under visible-light irradiation (>420 nm). The synergic effect of g-C_3N_4 and MoO_3 was considered as the origin of the high activity of MoO_3/g-C_3N_4 composite. However, due to the very low solubility of MoO_3, the deactivation of the photocatalyst in water is unavoidable. The photocatalyst containing MoO_3 might be more suitable for the air purification. In addition, the reactive species trapping experiment and the coumarin photoluminescence probing technique were used for verification of the Z-scheme mechanism of MoO_3/g-C_3N_4 composite. The method employed in this research could help researchers study the photocatalytic mechanism of new composite photocatalyst.

Acknowledgements

We acknowledge Dr. Xiaodong Yi in Xiamen University for his help in XPS analysis. This work was financially supported by the National Natural Science Foundation of China (21003109, 51108424), the Opening-foundation of State Key Laboratory Physical Chemistry and Solid Surfaces, Xiamen University, China (201311), and the School of Energy Resources at University of Wyoming

[a] *Department of Materials Physics, Zhejiang Normal University, Jinhua, China. Fax: +86-0579-83714946; Tel: +86-0579-83792294; E-mail: hym@zjnu.cn*
[b] *Institute of Physical Chemistry, Zhejiang Key Laboratory for Reactive Chemistry on Solid Surfaces, Zhejiang Normal University, Jinhua, China.*
[c] *College of Geography and Environmental Sciences, Zhejiang Normal University, Jinhua, China*
[d] *State Key Laboratory Physical Chemistry of Solid Surfaces, Xiamen University, Xiamen, China*
[e] *Department of Chemical & Petroleum Engineering, University of Wyoming, Laramie, Wyoming 82071, United States. Fax: +1-307-766-6667; Tel: +1-307-766-5633; E-mail: mfan@uwyo.edu*
[f] *School of Civil and Environmental Engineering, Georgia Institute of Technology, Georgia, 30332, United States. Fax: +1-404-894-8266; Tel: +1-404-385-4577; E-mail: mfan3@mail.gatech.edu*

† Electronic Supplementary Information (ESI) available: TG-DTA profiles of pure g-C_3N_4 and 1.5wt.% MoO_3/g-C_3N_4 composite (Fig. S1), SEM pictures of pure g-C_3N_4, MoO_3, and 1.5wt.% MoO_3/g-C_3N_4 composite (Fig. S2). XRD patterns of 1.5wt.% MoO_3/g-C_3N_4 before and after reaction (Fig. S3). The elemental concentration in 1.5 wt% MoO_3/g-C_3N_4 photocatalyst (Table S1). See DOI: 10.1039/b000000x/

Notes and references

1 S. Malato, J. Blanco, A. Vidal, C. Richter, *Appl. Catal. B: Environ.*, 2002, **37,** 1–15.
2 A. Fujishima, T.N. Rao, D.A. Tryk, *J. Photochem. Photobiol. C: Photochem. Rev.*, 2000, **1**, 1–21.
3 S.Kwon, M. Fan, A.T. Cooper, H. Yang, *Crit Rev. Env. Sci. Tec.*, 2008, **38**, 197–226.
4 J. Qu, M. Fan, *Crit Rev. Env. Sci. Tec.*, 2010, **40**, 519–560.
5 H. Hu, Q. Yang, X. Lu, W. Wang, S. Wang, M. Fan, *Crit Rev. Env. Sci. Tec.*, 2010, **40**, 452–518.

6 T. Li, Y. Chen, P. Wan, M. Fan, X. Yang, *J. Am. Chem. Soc.,* 2009, **132**, 2500–2501.

7 W. Choi, A. Termin, M.R. Hoffmann, *J. Phys. Chem.,* 1994, **98**, 13669–13679.

8 J. Zhang, C.X. Pan, P.F. Fang, J.H. Wei, R. Xiong, *ACS Appl. Mater. Inter.*, 2010, **2**, 1173–1176.

9 R. Ashi, T. Morikawa, T. Ohwaki, K. Aoki, Y. Taga, *Science*, 2001, **293**, 269–271.

10 G.H. Qin, Z. Sun, Q.P. Wu, L. Lin, M. Liang, S. Xue, *J. Hazard. Mater.*, 2011, **192**, 599–604.

11 J.B. Mu, B. Chen, M.Y. Zhang, Z.C. Guo, P. Zhang, Z.Y. Zhang, Y.Y. Sun, C.L. Shao, Y.C. Liu, *ACS Appl. Mater. Inter.*, 2012, **4**, 424–430.

12 A.K.P. Mann, E.M.P. Steinmiller, S.E. Skrabalak, *Dalton Trans.*, 2012, **41**, 7939–7945.

13 X.C. Wang, K. Maeda, A. Thomas, K. Takanabe, G. Xin, J.M. Carlsson, K. Domen, M. Antonietti, *Nat. Mater.,* 2009, **8**, 76–80.

14 Y.P. Bi, S.X. Ouyang, N. Umezawa, J.Y. Cao, J.H. Ye, *J. Am. Chem. Soc.*, 2011, **133**, 6490–6492.

15 P. Wang, B.B. Huang, X.Y. Zhang, X.Y. Qin, H. Jin, Y. Dai, Z.Y. Wang, J.Y. Wei, J. Zhan, S.Y. Wang, J.P. Wang, M.H. Whangbo, *Chem. Eur. J.*, 2009, **15**, 1821–1824.

16 S.C. Yan, Z.S. Li, Z.G. Zou, *Langmuir*, 2009, **25**, 10397–10401.

17 G.Q. Li, N. Yang, W.L. Wang, W.F. Zhang, *J. Phys. Chem. C*, 2009, **113**, 14829–14833.

18 Y.J. Cui, J.H. Huang, X.Z. Fu, X.C. Wang, *Catal. Sci. Technol.,* 2012, **2**, 1396–1402.

19 S.C. Lee, H.O. Lintang, L. Yuliati, *Chem. Asia J.,* 2012, **7**, 2139–2144.

20 G. Liu, P. Niu, C.H. Sun, S.C. Smith, Z.G. Chen, G.Q. Lu, H.M. Cheng, *J. Am. Chem. Soc.,* 2010, **132**, 11642–11648.

21 X.C. Wang, X.F. Chen, A. Thomas, X.Z. Fu, M. Antonietti, *Adv. Mater.*, 2009, **21**, 1609–1612.

22 S.C. Yan, S.B. Lv, Z.S. Li, Z.G. Zou, *Dalton Trans.*, 2010, **39**, 1488–1491.

23 Y.J. Wang, Z.X. Wang, S. Muhammad, J. He, *CrystEngComm,* 2012, **4**, 5065–5070.

24 J.H. Yang, H.J. Yan, X.L. Wang, F.Y. Wen, Z.J. Wang, D.Y. Fan, J.Y. Shi, C. Li, *J. Catal.,* 2012, **290**, 151–157.

25 L.Y. Huang, H. Xu, Y.P. Li, H.M. Li, X.N. Cheng, J.X. Xia, Y.G. Xu, G.B. Cai, *Dalton Trans.*, 2013, **42**, 8606–8616.

26 J.X. Sun, Y.P. Yuan, L.G. Qiu, X. Jiang, A.J. Xie, Y.H. Shen, J.F. Zhu, *Dalton Trans.*, 2012, **41**, 6756–6763.

27 T.T. Li, L.H. Zhao, Y.M. He, J. Cai, M.F. Luo, J.J. Lin, *Appl. Catal. B: Environ.,* 2013, **129**, 255–263.

28 L. Ge, C.C. Han, J. Liu, *Appl. Catal. B: Environ.*, 2011, **108**, 100–107.

29 H. Xu, J. Yan, Y.G. Xu, Y.H. Song, H.M. Li, J.X. Xia, C.J. Huang, H.L. Wan, *Appl. Catal. B: Environ.,* 2013, **129**, 182–193.

30 H.J. Yan, H.X. Yang, *J. Alloy Compd.*, 2011, **509**, L26–L29.

31 J. Cai, Y.M. He, X.X. Wang, L.H. Zhang, L.Z. Dong, H.J. Lin, L.H. Zhao, X.D. Yi, W.Z. Weng, H.L. Wan, *RSC Adv.*, 2013, **3**, 20862–20868.

32 K. Kondo, N. Murakami, C. Ye, T. Tsubota, T. Ohno, *Appl. Catal. B: Environ.*, 2013, **142–143**, 362–367.

33 L.Y. Huang, H. Xu, R.X. Zhang, X.N. Cheng, J.X. Xia, Y.G. Xu, H.M. Li, *Appl. Surf. Sci.*, 2013, **283**, 25–32.

34 Y.J. Wang, Y.M. He, T.T. Li, J. Cai, M.F. Luo, L.H. Zhao, *Chem. Eng. J.*, 2012, **189–190**, 473–481.

35 G.T. Li, K.H. Wong, X.W. Zhang, C. Hu, J.C. Yu, R.C.Y. Chan, P.K. Wong, *Chemosphere*, 2009, **76**, 1185–1191.

36 J. Cao, B.Y. Xu, B.D. Luo, H.L. Lin, S.F. Chen, *Appl. Surf. Sci.*, 2011, **257**, 7083–7089.

37 Q.J. Xiang, J.G. Yu, P.K. Wong, *J. Colloid Interf. Sci.*, 2011, **357**, 163–167.

38 Y.M. He, J. Cai, T.T. Li, Y. Wu, Y.M. Yi, L.H. Zhao, M.F. Luo, *Ind. Eng. Chem. Res.*, 2012, **51**, 14729–14737.

39 Y.M. He, J. Cai, T.T. Li, Y. Wu, H.J. Lin, L.H. Zhao, M.F. Luo, *Chem. Eng. J.*, 2013, **215–216**, 721–730.

40 T.H. Chiang, H.C. Yeh *Mater.* 2013, **6**, 4609**–**4625.

41 H.J. Yan, Y. Chen, S.M. Xu, *Int. J. Hydrogen Energ.*, 2012, **37**, 125–133.

42 F. Prinetto, G. Cerrato, G. Ghiotti, A. Chiorino, M.C. Campa, D. Gazzoli, V. Indovina, *J. Phys. Chem.*, 1995, **99**, 5556–5567.

43 B.M. Reddy, B. Chowdhury, E.P. Reddya, A. Fernández, *Appl. Catal. A: Gen.*, 2001, **213**, 279–288.

44 K. Asakura, K. Nakatani, T. Kubota, Y. Iwasawa, *J. Catal.,* 2000, **194**, 309–317.

45 Y.M. He, L.H. Zhao, Y.J. Wang, T.T. Li, T.H. Wu, X.T. Wu, Y. Wu, *Ind. Eng. Chem. Res.*, 2011, **50**, 7109–7119.

46 H.J. Dong, G. Chen, J.X. Sun, C.M. Li, Y.G. Yu, D.H. Chen, *Appl. Catal. B: Environ.*, 2013, **134–135**, 46–54.

47 S.M. Lam, J.C. Sin, A.Z. Abdullah, A.R. Mohamedt, *J. Mol. Catal. A: Chem.*, 2013, **370**, 123–131.

48 A. Chithambararaj, N.S. Sanjini, S. Velmathi, A.C. Bose, *Phys. Chem. Chem. Phys.*, 2013, **15**, 14761–14769.

49 S.C. Yan, Z.S. Li, Z.G. Zou, *Langmuir*, 2010, **26**, 3894–3901.

50 D.Z. Li, Z.X. Chen, Y.L. Chen, W.J. Li, H.J. Huang, Y.H. He, X.Z. Fu, *Environ. Sci. Technol.*, 2008, **42**, 2130–2135.

51 M. Kong, Y.Z. Li, X. Chen, T.T. Tian, P.F. Fang, F. Zheng, X.J. Zhao, *J. Am. Chem. Soc.*, 2011, **113**, 16414–16417.

52 Q.J. Xiang, J.G. Yu, M. Jaroniec, *J. Phys. Chem. C*, 2011, **115**, 7355–7363.

53 L.Y. Huang, H. Xu, Y.P. Li, H.M. Li, X.N. Cheng, J.X. Xia, Y.G. Xu, G.B. Cai, *Dalton Trans.*, 2013, **42**, 8606–8616.

54 B.J. Ma, J.S. Kim, C.H. Choi, S.I. Woo, *Int. J. Hydrogen Energ.*, 2013, **38**, 3582–3587.

55 M. Navgire, A. Yelwande, D. Tayde, B. Arbad, M. Lande, *Chin. J. Catal.,* 2012, **33**, 261–266.

56 Y. Sasaki, H. Nemoto, K. Saito, A. Kudo, *J. Phys. Chem. C,* 2009, **113**, 17536–17542.

57 P. Ye, J.J. Xie, Y.M. He, L. Zhang, T.H. Wu, Y. Wu, *Mater. Lett.*, 2013, **108**, 168–171.

58 J. Liang, Y.Q. Cao, H. Lin, Z.Z. Zhang, C.C. Huang, X.X. Wang, *Inorg. Chem.,* 2013**, 52,** 6916–6922.

59 Y.M. He, J. Cai, T.T. Li, Y. Wu, H.J. Lin, L.H. Zhao, M.F. Luo, *Chem. Eng. J.,* 2013, **215-216,** 721–730.

60 H.H. Ji, F. Chang, X.F. Hu, W. Qin, J.W. Shen, *Chem. Eng. J.*, 2013, **218**, 183–190.